


 Cite this: *Lab Chip*, 2021, 21, 3762

## A bioinspired, passive microfluidic lobe filtration system†

 Andrew S. Clark and Adriana San-Miguel \*

Size-based microfluidic filtration systems can be affected by clogging, which prevents their use in high-throughput and continuous applications. To address these concerns, we have developed two microfluidic lobe filters bioinspired by the filtration mechanism of two species of manta ray. These chips enable filtration of particles around 10–30  $\mu\text{m}$  with precise control and high throughput by using two arrays of equally spaced filter lobes. For each filter design, we investigated multiple inlet flow rates and particle sizes to identify successful operational parameters. Filtration efficiency increases with fluid flow rate, suggesting that particle inertial effects play a key role in lobe filter separation. Microparticle filtration efficiencies up to 99% were obtainable with inlet flow rates of 20  $\text{mL min}^{-1}$ . Each filter design successfully increased microparticle concentrations by a factor of two or greater at different inlet flow rates ranging from 6–16  $\text{mL min}^{-1}$ . At higher inlet flow rates, ANSYS Fluent simulations of each device revealed a complex velocity profile that contains three local maxima and two inflection points. Ultimately, we show that distances from the lobe array to the closest local maxima and inflection point of the velocity profile can be used to successfully estimate lobe filtration efficiency at each operational flow rate.

 Received 23rd May 2021,  
 Accepted 5th August 2021

DOI: 10.1039/d1lc00449b

[rsc.li/loc](https://rsc.li/loc)

## 1. Introduction

Size-based microparticle filtration is used in applications with widely different scales. Research and clinical microparticle manipulation applications often separate or filter samples with volumes of approximately 1–1000  $\mu\text{L}$  in size,<sup>1–3</sup> while industrial applications often filter volumes greater than 1 L.<sup>4,5</sup> Currently, size-based microparticle filters are made of a mesh sieve, which intercept particles larger than the pore size. Due to the inherent nature of these filters, they commonly clog and require an operator to either change or clean the filter,<sup>6</sup> which ultimately decreases microparticle separation throughput.

Microfluidic devices offer promising advantages for microparticle filtration as they enable precise manipulation of fluids, and therefore microparticle suspensions, within channels with dimensions around 1–1000  $\mu\text{m}$ .<sup>7,8</sup> Microfluidic filters are commonly split into two groups: active and passive filtration. Active microfluidic filters connect the microfluidic device to external equipment, which then relies on external force fields, such as acoustics<sup>9,10</sup> or magnetics<sup>11</sup> to manipulate particles. These technologies usually require

particle pre-treatment, as well as complex and expensive external hardware, making them less attractive for high-throughput applications.

Conversely, passive microfluidic filters do not rely on active external fields and are often praised for their simplicity. These filters utilize different methods, such as deterministic lateral displacement,<sup>12</sup> cross-flow filtration,<sup>13,14</sup> and membrane filtration.<sup>15</sup> These methods have all been shown to perform microparticle filtration with adequate efficiency; however, each is limited by throughput. For instance, deterministic lateral displacement must be operated at precise and slow flow rates ( $\sim 10 \mu\text{L min}^{-1}$ ) to reach efficient separation,<sup>12</sup> while membrane filters and cross-flow filtration are plagued by the possibility of clogging since particles are larger than the filter pore size.<sup>15,16</sup>

Another option for microparticle filtration within microfluidic devices is inertial particle separation. Unlike many microfluidic devices that operate at very low Reynolds Numbers ( $\text{Re} = \rho UH/\mu$ ; where  $\rho$  is fluid density,  $U$  is average flow velocity,  $H$  is hydraulic diameter, and  $\mu$  is fluid viscosity;  $\text{Re} \rightarrow 0$ ), inertial microfluidics considers the nonlinear effects that fluid inertia has on microfluidic systems that operate under intermediate laminar flow.<sup>17–19</sup> Inertial particle separation relies on a balancing act of two main forces, the shear-induced lift and the wall-induced lift, to precisely manipulate microparticles based on size.<sup>8</sup> The resulting net, inertial lift force is dependent on  $\text{Re}$  and particle position

Department of Chemical & Biomolecular Engineering, North Carolina State University, Raleigh, NC, USA. E-mail: [asanmig@ncsu.edu](mailto:asanmig@ncsu.edu)

† Electronic supplementary information (ESI) available. See DOI: 10.1039/d1lc00449b

within the channel, as well as directly proportional to the product of shear rate and shear gradient.<sup>20–23</sup> Thus, if the signs of shear rate and shear gradient are different, the resulting inertial lift force could change direction.<sup>20,21</sup> Since the inertial lift force is highly dependent on fluid flow velocity ( $Re$ ), inertial microfluidic filters are often limited by finding a Goldilocks flow rate (not too fast or slow).<sup>19,23–28</sup>

In a straight channel, particle equilibrium positions are determined by cross-section geometry, particle size, and flow rate.<sup>21,29,30</sup> Channel geometry and an introduction of a secondary flow can thus significantly alter particle

equilibrium position. Secondary flow, which is a minor flow perpendicular to the primary flow, helps reduce the number of equilibrium positions by applying an additional drag force to help control particle location.<sup>18</sup> Most state-of-the-art inertial particle separation technologies utilize secondary flows to increase particle filtration efficiency. These devices are commonly separated into groups based on their strategy of controlling secondary flow (expansion–contraction arrays, spiral, or sinusoidal devices).<sup>15,19,21,24,26,30–34</sup> In all cases, smaller particles experience greater effects from the secondary flow. Using these principles, inertial microfluidics

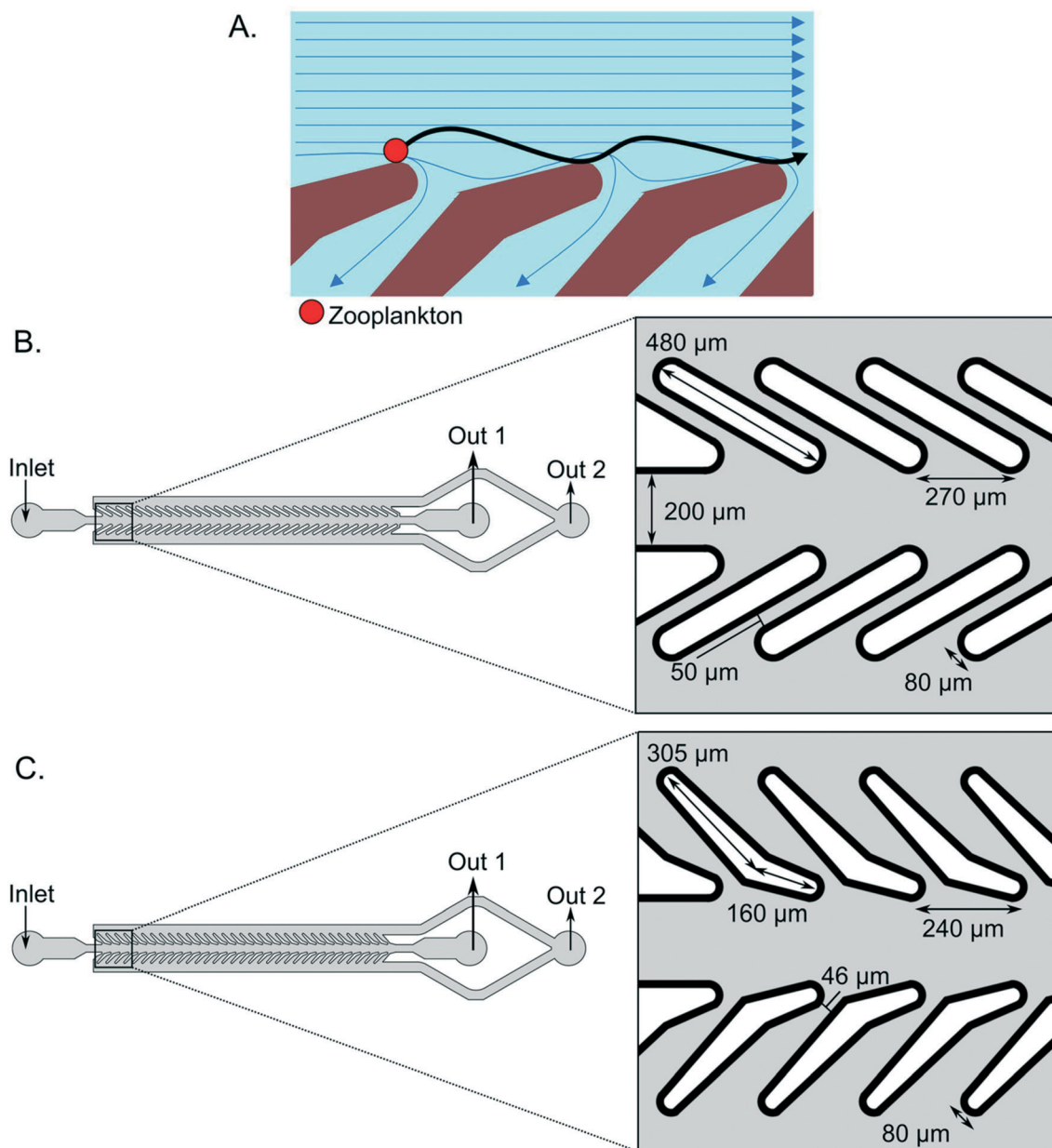


**Fig. 1** A. Cartoon schematic portraying how both species of the manta ray feed on zooplankton. Blue arrows indicated fluid flow direction and the black arrow represents an example particle path. The lobe design shown is based on the *M. tarapacana*. B. Schematic of the oblong lobe microfluidic device based on the *M. birostris* lobe design. Dimensions of the main channels are shown in the inset image with a total device height of  $60\ \mu\text{m}$ . C. Schematic of the bent lobe microfluidic device based on the *M. tarapacana* lobe design. Dimensions of the main channels are shown in the inset image with a total device height of  $60\ \mu\text{m}$ . The main channel is  $200\ \mu\text{m}$  in width.

applications include bacteria and tumor cell aggregate filtration,<sup>19,35,37</sup> as well as debris removal for membrane-free sample cleaning.<sup>49</sup>

Recently, biomimicry, or the emulation of elements of nature to solve complex problems, has significantly advanced multiple technologies. Interestingly, Divi *et al.* recently explored the manta ray, specifically *M. birostris* and *M. tarapacana*'s, filter feeding mechanism: lobe filtration. These animals use an array of nonstick filter lobes to capture zooplankton while swimming.<sup>38</sup> The main difference between the two species includes a slight difference in lobe design, which permits the *M. tarapacana* to feed at nearly seven times smaller pressure head.<sup>38</sup> Unlike most filter feeding marine life, these animals continuously feed on particles smaller than their filter's pore size by using precisely spaced filter lobes.<sup>38</sup> These lobes, which are separated by  $\sim 340\ \mu\text{m}$ ,<sup>39</sup> cause fluid to quickly change directions, creating a secondary flow. At adequate bulk flow rates, larger particles diverge from fluid streamlines and continue their inertial path, resulting in a non-clogging filtering mechanism with attributes similar to inertial particle separation, which can be better visualized in Fig. 1A. Interestingly, both *M. birostris* and *M. tarapacana* can capture zooplankton using this mechanism, where efficiency increases with particle size and bulk fluid Re.<sup>39,40</sup> Moreover, Divi *et al.* noted that increased swimming speeds with  $\text{Re} > 1000$ , do not affect filtration efficiency.<sup>38</sup> Nevertheless, obtaining  $\text{Re} \sim 1000$  in a microfluidic device is often difficult due to the proportional relationship between channel dimensions and Re. Thus, scaling down lobe filtration to a microfluidic device capable of filtering smaller particles ( $\sim 10\ \mu\text{m}$ ) with high efficiencies may be difficult.

In this work, we sought to demonstrate that lobe filtration, bioinspired by both *M. birostris* and *M. tarapacana*, can be scaled down to a microfluidic device to create a high throughput microparticle filter capable of filtering particles on the order of  $10\ \mu\text{m}$  with processing speeds up to  $20\ \text{mL min}^{-1}$  in a single device. We designed and characterized two filter designs based on the lobe structures of *M. birostris* and *M. tarapacana* (named oblong lobe and bent lobe, respectively) by running  $25\ \mu\text{m}$  and  $15\ \mu\text{m}$  particles through the devices at varying flow rates, showing passive lobe filtration's potential for wide-ranged applications. We further explored the effect that particle size has on lobe filtration efficiency by processing particle suspensions at various inlet flow rates for both designs. Moreover, by utilizing ANSYS Fluent simulations, we revealed an unexpected, complex velocity profile for microfluidic flow, which contains multiple velocity local maxima and inflection points. In the region between the velocity local maxima and the inflection point, the inertial lift force changes direction. We obtained the distances between the lobes and location in the main channel of the velocity local maxima and the inflection point. Comparing these distances to various particle sizes with experimentally obtained efficiencies revealed a

simple and robust explanation for microfluidic lobe filtration success.

## 2. Materials and methods

### a. Design and fabrication of microfluidic devices

Both microfluidic filter devices used in this study were designed and fabricated through standard photo and soft-lithography techniques. Designs were drawn in AutoCAD 2018 drafting software (Autodesk). Transparency films from the designs were printed by FineLine Imaging. SU-8 2025 (Kayaku Advanced Materials, Inc.) negative photoresist was spun at 1500 rpm to obtain a  $60\ \mu\text{m}$  layer on a 4 inch silicon wafer. We noticed that low and gradual bake times significantly improved master mold resolution. Therefore, the wafer was then soft baked by gradually increasing a room temperature hot plate to  $65\ ^\circ\text{C}$ , holding for 10 minutes, then increasing the hotplate to  $95\ ^\circ\text{C}$  and holding for 30 minutes. The wafer was then allowed to cool to room temperature on the hot plate. Following the soft bake, the wafer was exposed to UV light masked by the photomask for 6 seconds in a Kloe UV-KUB 3 mask aligner. The wafer was then baked with the same procedure as the previous soft bake to ensure complete cross-linking of exposed areas. The wafer was then shaken in SU-8 developer for 20 minutes to remove unexposed SU-8. The device was hard baked at  $200\ ^\circ\text{C}$  for 2 minutes then placed in a vacuum chamber with a few drops of trichloro-perfluorooctyl-silane overnight to avoid irreversible adhesion of PDMS to SU-8 photoresist. A 9:1 ratio of polymer to crosslinker of polydimethylsiloxane (PDMS) was used for soft lithography. The polymer/crosslinker mixture was mixed and degassed to remove bubbles prior to pouring on the microfluidic mold. The PDMS was then cured at  $80\ ^\circ\text{C}$  for 2 hours prior to peeling. Individual filters were then cut and punched with a sharpened  $0.44\ \text{mm}$  dispensing needle (McMaster-Carr). Devices were bonded to  $22 \times 50\ \text{mm}$  glass slides in an  $\text{O}_2$  plasma chamber. Finally, tubing was attached to each inlet and outlet on the devices.

### b. Preparation of particles

Particle suspensions were made using various concentrations and particle sizes. Device characterization experiments used  $25\ \mu\text{m}$  red fluorescent particles (Fisher Scientific, Inc.) (Ex:  $542\ \text{nm}$ , Em:  $612\ \text{nm}$ ) and  $15\ \mu\text{m}$  green fluorescent particles (Fisher Scientific, Inc.) (Ex:  $468\ \text{nm}$ , Em:  $508\ \text{nm}$ ), which were diluted using  $0.1\%$  w/v Triton TX100-water solution to  $\sim 10^6$  particles per mL and  $\sim 5 \times 10^6$  particles per mL, respectively. Low concentration experiments were conducted with  $\sim 10^4$  particles per mL of  $25$  and  $15\ \mu\text{m}$  particles, while high concentration experiments used  $10^7$  particles per mL. Particle range experiments using green fluorescent particles (Cospheric LLC) (Ex:  $468\ \text{nm}$ , Em:  $508\ \text{nm}$ )  $10\text{--}29\ \mu\text{m}$  in size were diluted to  $\sim 10^6$  particles per mL with a  $0.1\%$  w/v Triton X-100 water solution. Particle suspensions were mixed with a vortex mixer for 1 minute prior to use within filter devices.

### c. Experimental set up

Each microfluidic lobe filter was tested by flowing fluorescent particles through the device and analyzing steady state operation, as well as particle concentrations in both outlets. Steady state operation was achieved when there was no discernable change in particle tracks under operator observation. Particle suspensions were inserted into the device through a syringe pump (Harvard Apparatus) and a 10 mL syringe (BD Plastic). Inlet flow rates depended on experiment type and filter design. Most experiments with the oblong lobe device used flow rates of 1, 2, 4, 6, 8, 10, 12, and 16 mL min<sup>-1</sup>. Most experiments with the bent lobe device used inlet flow rates of 1, 2, 4, 6, 8, 12, 16, and 20 mL min<sup>-1</sup>. Inlet samples were taken before each experiment and outlets were collected for later analysis of particle concentrations. Fluorescent images of steady state operation were taken using Infinity Capture and a Lumenera Infinity3 color CCD camera on a Leica M165 FC microscope using a dual band pass filter in fluorescence mode with a metal halide light source.

### d. Image processing and characterization

Filtration experiments using 25 μm and 15 μm particles were characterized by obtaining particle counts from the inlet and both outlets for each experimental parameter. Images of 1 μL samples pressed between two glass slides were taken on a Leica M165 FC with Infinity Capture software and Lumenera Infinity3 color CCD camera at 7.3× magnification. A custom-written MATLAB image processing code enabled particle counting to obtain concentrations at the inlet and outlets. This code separated images into red and green channels to analyze 25 μm and 15 μm particle counts separately. These images were then binarized using the “imbinarize” function in MATLAB. The resulting binary object sizes were obtained using “regionprops” function. If a binary object's area (in pixels) was within the corresponding range for the current particle size analysis, it was counted toward the particle count. Three images were processed for each experimental condition.

Similarly, particle size range experiments utilized images of samples taken at the inlet and both outlets. Samples were prepared by placing 1 μL droplets on a glass slide and imaging the droplets with an inverted Leica DMi8 widefield fluorescence microscope equipped with a Lumencor Spectra X fluorescent LED light source and Hamamatsu Orca-Flash4.0 camera at 10× magnification. Three images were taken for each inlet and outlet for each experiment. Images were then processed using a custom written MATLAB image processing algorithm to find circles and measure the radius. Particle counts were placed in 5 μm bins ranging from 10–30 μm. Each bin size was then analyzed separately for efficiency.

Each filter design was characterized for particle filtration efficiency and particle concentration ratio as others have done<sup>38,41,42</sup> using particle counts obtained from the image processing algorithms. In each case, efficiency was calculated as:

$$\text{Efficiency} = \left( 1 - \frac{(\text{Out 2 Concentration})}{(\text{Inlet Concentration})} \right) \times 100\% \quad (1)$$

where out 2 refers to the peripheral device outlet, intended for the filtrate.

Concentration ratio was calculated as:

$$\text{Concentration Ratio} = \frac{\text{Out 1 Concentration}}{\text{Inlet Concentration}} \quad (2)$$

where out 1 refers to the center device outlet, intended for particle collection.

### e. Velocity profile simulations and analysis

Velocity profiles within each filter design were obtained using ANSYS Fluent 19.1 computational fluid dynamics simulation software. Three-dimensional microfluidic filter designs were exported from AutoCAD as ACIS files and subsequently loaded into the ANSYS Fluent graphical user interface (GUI). Each design was split into five parts to permit finer meshing (7 μm element size; cartesian meshing method in ANSYS Meshing) in the center channel (ESI† S1.A and S1.B). Steady state simulations (with 500 iterations) were conducted using standard water properties for the fluid, as well as a laminar flow model with the SIMPLE solver. Velocity inlet boundary conditions were used (1 mL min<sup>-1</sup> to 20 mL min<sup>-1</sup>) with zero-gauge pressure outlets. A residual convergence criterion of 10<sup>-5</sup> was used. A mesh independence study was conducted using outlet mass flux to ensure mesh performance (ESI† S1.C). Following simulations, velocity values from the  $z = 30$  μm plane were exported as ASCII files and subsequently imported into MATLAB. The imported velocity values ( $x$ ,  $y$ ,  $z$ , and magnitude) were then segregated by their  $x$ -coordinate corresponding to each filter lobe in the design to obtain velocity profiles along the device. Smooth profiles were obtained by interpolating between points within the main channel using the “interp1” function in MATLAB. Velocity profiles were then analyzed using a custom MATLAB algorithm.

All custom code is available at GitHub (<https://github.com/asanmiguel/MantarayFilter>).

## 3. Results and discussion

### a. Device designs

The lobe structures of *M. birostris* and *M. tarapacana* inspired the designs of the oblong lobe and bent lobe microfluidic devices, respectively. Using the dimensions listed by Divi *et al.* as a basis,<sup>38</sup> the lobe dimensions were scaled down by approximately 6 times to aim for a target particle filtration size of 10–30 μm. The target filtration size was chosen for its multiple real-world applications, such as cell aggregation filtration<sup>36,37</sup> and microplastic removal.<sup>44,45</sup> Each design had similar features including one inlet that throttles to a center channel with an array of equally spaced lobes on each side, and two outlets (Fig. 1B and C). Since lobe filtration had not yet been conducted in a microfluidic device, there

were many potential parameters that could influence filtration success including lobe design, lobe angle, lobe width, lobe separation, center channel dimension, among others. Thus, both the oblong and bent lobe design dimensions were obtained by scaling down previously reported measurements of *M. birostris* and *M. tarapacana*.<sup>38</sup> The oblong lobe device included lobes of 480  $\mu\text{m}$  in length

and 80  $\mu\text{m}$  in width, separated by 50  $\mu\text{m}$ , with a 30 degree orientation. Each array of lobes contained 31 individual lobes to provide ample opportunities for microparticle filtration (Fig. 1B). Since both *M. birostris* and *M. tarapacana* feed successfully at moderate Reynold's number flow ( $Re \sim 1000$ ), we hypothesized that a similar  $Re$  would be necessary for microfluidic filtration success. Hence, center channel

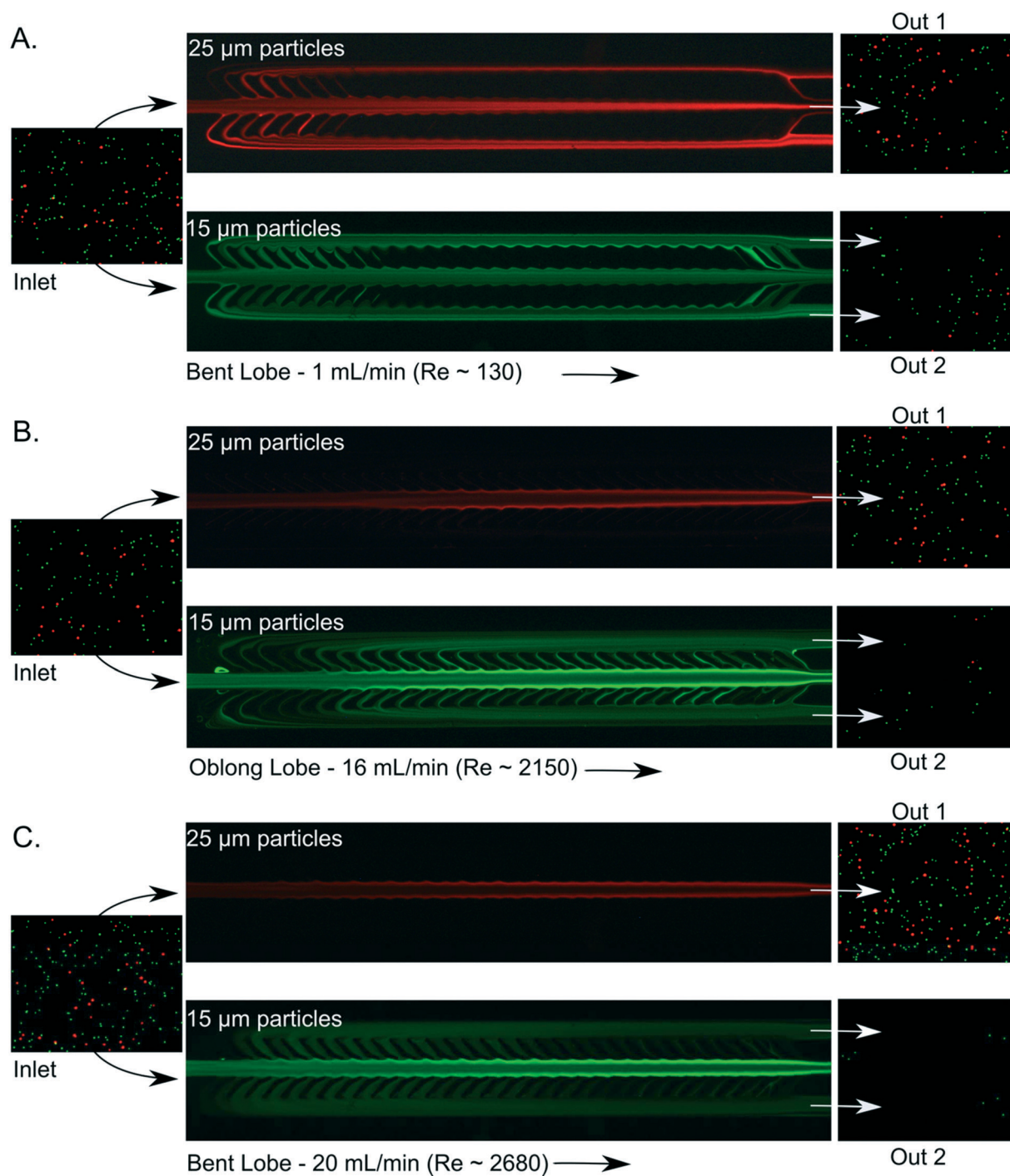


**Fig. 2** Representative steady state device operation with example inlet and outlet images for the A. bent lobe device at  $1 \text{ mL min}^{-1}$ , B. oblong lobe device at  $16 \text{ mL min}^{-1}$ , and C. bent lobe device at  $20 \text{ mL min}^{-1}$ . Red and green channel images depict the particle tracks for 25  $\mu\text{m}$  particles and 15  $\mu\text{m}$  particles, respectively. Particle count images have both channels overlapped to easily compare particle concentrations.

dimensions were designed to permit high flow rates ( $\sim 200 \mu\text{m}$  in width by  $60 \mu\text{m}$  in height).

The bent lobe design has similar dimensions with the key design change being the shape of the lobe. The lobe design, seen in Fig. 1C, features a bend approximately one third from the top of the lobe, causing the angle the lobe to be closer to the horizontal of the center channel and the minimum distance between lobes to be slightly closer ( $\sim 4 \mu\text{m}$ ). Like the oblong lobe design, the other dimensions selected were intended to obtain moderate Re flow in the center channel.

### b. Lobe filtration operation

Both filter lobe designs were tested for their ability to filter and/or concentrate large particles of  $25 \mu\text{m}$  and  $15 \mu\text{m}$  at several inlet flow rates. Mixed particle suspensions were pumped at different inlet flow rates through each filter design using a syringe pump to test both particle sizes concurrently, removing the need for extra experiments. Since the  $25 \mu\text{m}$  and  $15 \mu\text{m}$  particles were fluorescently labeled in different colors (red and green, respectively), size-based particle tracks were visualized within the device using a fluorescent dissecting scope. At slow inlet flow rates with  $Re \sim 130$  (Fig. 2A), both  $25 \mu\text{m}$  and  $15 \mu\text{m}$  particles leave from the center channel through the first few lobe pores and into the outer channel. We observed that particles appear to return from the outer channels into the main channel and exit into out 1 for both particle sizes. We hypothesize that the particles that return into the main channel are simply following fluid path lines, since it appears that only some particles closest to the lobes return to the main channel. This phenomenon of particles returning into the main channel was observed in both device designs.

To test the filter at higher Re within each device, we gradually increased the inlet flow rates until the syringe pump did not have enough power to flow fluid at the desired rate. These inlet flow rates ( $16 \text{ mL min}^{-1}$  for the oblong lobe and  $20 \text{ mL min}^{-1}$  for the bent lobe) were then determined to be the maximum inlet flow rate for each device. It is important to note that neither filter broke from too much pressure, suggesting that higher inlet flow rates could be achieved with a stronger syringe pump. At higher inlet flow rates, the steady state particle tracks significantly changes. The particle tracks at the maximum inlet flow rate for the oblong lobe and bent lobe devices can be observed in Fig. 2B and C, respectively. In both cases,  $25 \mu\text{m}$  particles (red channel) appear to be enter evenly dispersed throughout the channel. As the particles travel along the devices, they eventually stabilize near the edge of the main channel (by the lobe arrays) without exiting through the lobe pores. By contrast, a portion of the  $15 \mu\text{m}$  particles appear to exit through each of the filter lobes. Once  $15 \mu\text{m}$  particles exit through the filter pores, a majority stay in the outer channel and exit through out 2. Although, like particles in slow flow operation, a small portion of  $15 \mu\text{m}$  particles appear to return to the main channel at the last filter pore. We also ensured

particle track changes were a result of the lobes and not of solely inertial forces, as we tested the same channel design with no lobes (ESI† S2). As expected, no particle filtration was observed in the design with no lobes. Notably, steady state operational images of both lobe filter designs demonstrated successful filtration of  $25 \mu\text{m}$  particles and partial filtration of  $15 \mu\text{m}$  particles.

### c. Lobe filtration characterization

To quantify filtration efficiency and concentration capability, samples of the inlet and both outlets were collected and imaged for each experiment. Using these images, particle concentrations could be obtained and filtration efficiencies for both particle sizes and lobe designs could be calculated. Filtration efficiencies were grouped into three main categories for quick visualization of filter performance. The three categories include low (0–60%), moderate (60–90%), and high filtration (>90%), which are represented in Fig. 3A by the red, yellow, and green backgrounds, respectively. A filtration efficiency of 0% indicates no change in particle concentration between the inlet and out 2 suspensions. The grey background and negative efficiencies in Fig. 3A represent a higher concentration of particles in the filtrate (out 2) compared to the inlet. At common inertial particle flow rates ( $\sim 1 \text{ mL min}^{-1}$ ), both filters perform poorly with low efficiencies under 40%. Interestingly, both device designs have sharp increases in efficiency at a  $4 \text{ mL min}^{-1}$  inlet flow rate, indicating a change in forces experienced by particles within each device. At inlet flow rates higher than  $4 \text{ mL min}^{-1}$ , the bent lobe device obtains much higher filtration efficiencies for  $25 \mu\text{m}$  particles compared to the oblong lobe design. In this range ( $4 \text{ mL min}^{-1}$  to  $20 \text{ mL min}^{-1}$ ), the bent lobe device offers high filtration efficiencies with a maximum near 99%. Remarkably, this design can successfully process up to  $20 \text{ mL min}^{-1}$  of a  $25 \mu\text{m}$  particle suspension, which correlates to a clean filtrate (out 2) flow rate of approximately  $10 \text{ mL min}^{-1}$ . On the other hand, the oblong lobe design operates with moderate  $25 \mu\text{m}$  filtration efficiencies over these flow rates (up to  $16 \text{ mL min}^{-1}$ ) with maximum filtration efficiency of 88%. Moreover, the oblong lobe design appears to experience a slight decrease filtration efficiency with inlet flow rates over  $10 \text{ mL min}^{-1}$ , which is not observed with the bent lobe design. Ultimately, the oblong lobe design obtained clean filtrate flow rates from approximately  $3\text{--}8 \text{ mL min}^{-1}$  leaving out 2, as compared to clean filtrate flows of  $2\text{--}10 \text{ mL min}^{-1}$  for the bent lobe design.

As expected, both lobe filters designs performed worse with  $15 \mu\text{m}$  particles. The oblong lobe design operated with low efficiencies throughout all inlet flow rates with a maximum efficiency near 41%. In fact, the oblong lobe design appears to slightly increase  $15 \mu\text{m}$  particle concentration in the filtrate outlet when operated at  $1 \text{ mL min}^{-1}$ . However, the bent lobe design offered moderate

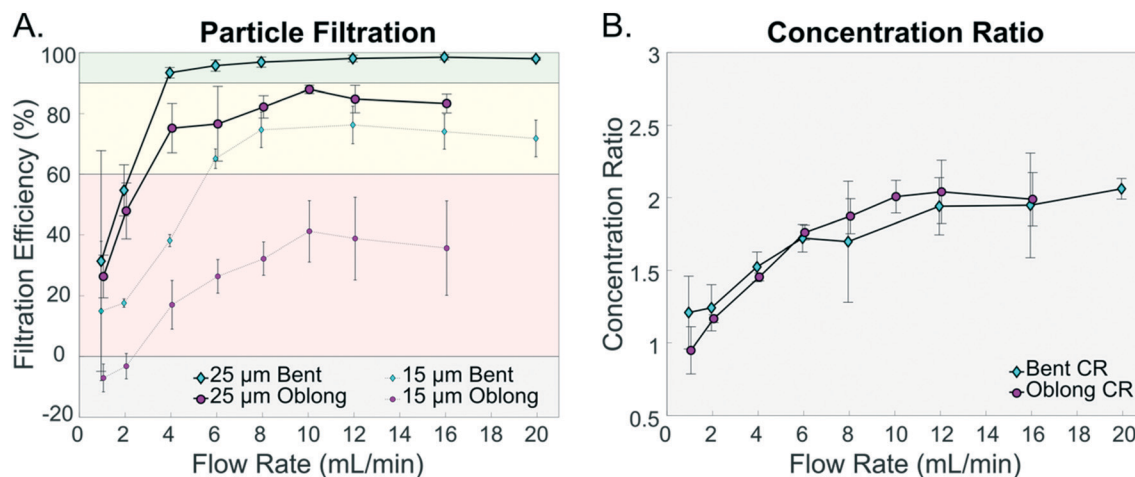


**Fig. 3** A. Microparticle filtration efficiencies for both the oblong lobe (purple circle) and bent lobe filter (blue diamond) designs over various inlet flow rates. The solid lines indicate 25 μm filtration efficiencies while the dashed line represents 15 μm filtration efficiencies (standard deviation as error bars,  $N = 3$ ). The red, yellow, and green shaded backgrounds represent low (0–60%), moderate (60–90%), and high (>90%) filtration efficiency regions, respectively. The grey background indicates a negative efficiency, meaning particle concentrations are higher in out 2 than in the inlet. B. Concentration ratio results (standard deviation as error bars,  $N = 3$ ) for the oblong lobe (purple circle) and bent lobe (blue diamond) designs over various inlet flow rates. A CR greater than 1 indicates a higher concentration in out 1 compared to the starting concentration.

filtration efficiencies of 75% for 15 μm particles at flow rates over 6 mL min<sup>-1</sup>, which provides evidence that lobe filtration does not have a binary particle cutoff size for successful filtration.

Continuous microparticle filters are also commonly used to concentrate sample particles of interest. Therefore, each lobe design was tested for its ability to concentrate particles within this size range. Fig. 3B shows the concentration ratio (CR) of 25 μm particles for each device at various flow rates (see Materials and methods for calculation equation). Almost every flow rate tested successfully concentrated particles. As inlet flow rates and particle filtration efficiencies increased, concentration ratios increased until an eventual plateau of 2.05 at 12 mL min<sup>-1</sup> for the oblong lobe design. Although filtration efficiencies steadied around 8 mL min<sup>-1</sup>, proportionally more fluid exits through out 2 with increasing inlet flow rates (ESI† S3), which ultimately increases particle CR. The bent lobe design offers similar CR at comparatively higher flow rates. We hypothesize that a higher inlet flow rate is needed to obtain similar CR values with the bent lobe design, since it operates with proportionally more fluid exiting through out 1 when holding the inlet flow rates constant (ESI† S3). At higher flow rates, the bent lobe design achieves >98% filtration efficiencies, permitting increased concentration ratios. In either case, microfluidic lobe filtration may also be used to concentrate particles at high processing flow rates.

Since the bent lobe design significantly improved particle filtration performance, we investigated changing other lobe design parameters (ESI† S4). We changed lobe spacing to 30 μm, lobe length to 600 μm, or lobe width to 150 μm, and measured particle filtration performance at an 8 mL min<sup>-1</sup> inlet flow rate (ESI† S5). Decreasing the lobe spacing to 30 μm was the only design change that offered improved

filtration performance with an efficiency comparable to the bent lobe design. However, since the filter pores in this design are much closer in size to the tested microparticles, the 30 μm spacing may be more prone to clogging and act similarly to a crossflow filter. Therefore, compared to the original oblong lobe design, the bent lobe design is the preferred modification for improved particle filtration performance.

Device performance across varying particle concentrations is important for potential filtration applications. Therefore, we tested both the oblong and bent lobe designs at low (10<sup>4</sup> particles per mL) and high (10<sup>7</sup> particles per mL) concentrations using previously determined successful operational flow rates. In both cases, particle concentration has no effect on successful particle filtration at 6 and 16 mL min<sup>-1</sup> for the oblong lobe design and 6 and 20 mL min<sup>-1</sup> for the bent lobe design (ESI† S6). Thus, lobe filtration may be applied to applications with wide-ranging particle concentrations.

Both the oblong lobe filter and bent lobe filter designs are successful at filtering and/or concentrating 25 μm particles. The bent lobe design offers slightly higher filtrate purity, while the oblong lobe design offers increased 15 μm particle filtrate recovery rates (ESI† S7). Moreover, the bent lobe device excels at filtration with highly efficient operation from 4 mL min<sup>-1</sup> up to 20 mL min<sup>-1</sup>. Given typical sizes of single cells obtained from tissue dissociation are around 15 μm, the high filtrate purity for this particle size (~99%) makes upstream processing for single cell analysis a promising application of this device, such as MCF-7 cell aggregate filtration.<sup>36</sup> However, the oblong lobe design offers increased 15 μm particle filtrate recovery rates and similar concentration ratios at slower inlet flow rates, which may be useful for sensitive applications that require operation with minimal shear forces.

#### d. Particle size significantly effects lobe filtration efficiency

To test how particle size affects lobe filter operation, we flowed various particle sizes (10–29  $\mu\text{m}$  particles) at different flow rates through each device and compared outlet concentrations for each size. For each design, particle range suspensions were injected into the device at the following flow rates: 2, 4, 6, 10, 14, and 18 (bent lobe only)  $\text{mL min}^{-1}$ . Samples of the inlets and both outlets were then imaged as detailed in the Materials and methods section. A custom-written image processing algorithm was then used to detect microparticles of various sizes (ESI† S8). In short, the algorithm binarized the fluorescent images and detected circles with radii within a predetermined size range. Detected particles were then binned based on diameter into 5  $\mu\text{m}$  bins and counted for efficiency analysis.

The efficiency curves based on 5  $\mu\text{m}$  particle size bins for the oblong lobe can be visualized in Fig. 4A. As expected, filtration efficiency increases with increasing particle size. However, there is no apparent difference in efficiency between the 10–15  $\mu\text{m}$  and 15–20  $\mu\text{m}$  bins, indicating that particle size may only affect filtration efficiency beyond a certain threshold size. Moreover, holding particle size constant, filtration efficiency increases with increasing inlet flow rates, which matches previous experimental observations (Fig. 3A). The low efficiency (0–60%), moderate efficiency (60–90%), and high efficiency (>90%) regions are indicated by the red, yellow, and green backgrounds in Fig. 4, respectively. For the oblong lobe design, particles in the low efficiency particle size range (10–20  $\mu\text{m}$ ) experience only slight increases in filtration efficiencies with increasing inlet flow rates. We hypothesize that some particles in this size range may never have an opportunity to leave through the filter pores due to small transverse velocities compared to the bulk flow direction, and thus experience increased

filtration efficiency with increasing flow. Particles in the 20–25  $\mu\text{m}$  size range can achieve moderate efficiencies, which suggests that particles of this size are large enough to experience different hydrodynamic lift forces within the filter. The increase in filtration efficiency of 25–30  $\mu\text{m}$  particles to >90% provides more evidence for this hypothesis. Interestingly, efficiencies near 100% were not reached with the tested particle size range in the oblong design.

Binned particle filtration efficiencies for the bent lobe design can be seen in Fig. 4B. Like the oblong lobe design, particle filtration efficiency in the bent lobe design increases with increasing particle size and increasing flow rates. However, no particle sizes tested resulted in low efficiencies, which suggests that even the smallest particles (10–15  $\mu\text{m}$ ) experience some hydrodynamic lift forces keeping them in the main channel in this filter design. Moreover, 15–20  $\mu\text{m}$  particles achieve mostly moderate efficiencies with a maximum of 93% at 10  $\text{mL min}^{-1}$ , while particles larger than 20  $\mu\text{m}$  reach efficiencies near 99%, indicating these particles experience strong lift forces keeping them from exiting through the filter lobe pores.

#### e. Velocity field simulations reveal velocity profile with inflection points

The multiple forces particles experience in microchannels can be estimated and explained by various aspects of the velocity field, such as the boundary layer location<sup>46</sup> and the saddle point<sup>41–43</sup> within the device. Since inertial lift coefficient, and thus the forces acting on the particles, is proportional to the product of the shear rate and the shear gradient,<sup>20,22</sup> estimating the velocity profile within the device seemed a necessary first step to understand microfluidic lobe filtration. We opted to obtain the velocity profile at the experimental inlet flow rates from computational fluid

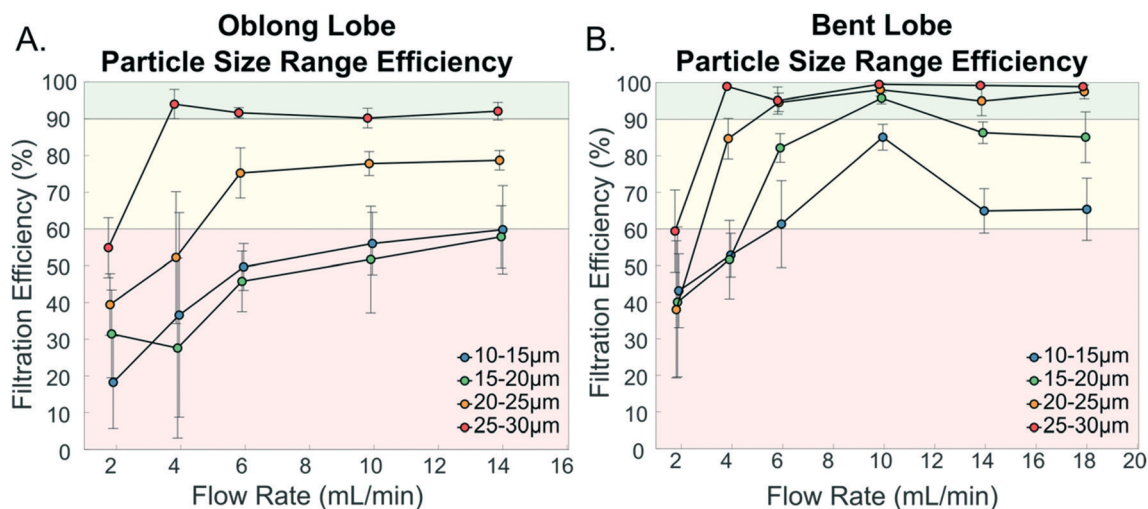


Fig. 4 Filtration efficiency (standard deviation error bars,  $N = 3$ ) for particles ranging from 10 to 30  $\mu\text{m}$  in diameter for the A. oblong lobe design and B. bent lobe design. Particles were binned by size into groups of 5  $\mu\text{m}$ . The red, yellow, and green backgrounds indicate low (0–60%), moderate (60–90%), and high (>90%) filtration efficiency regions, respectively.

dynamics simulations run in ANSYS Fluent 19.1 for both the oblong and bent lobe designs. The mesh for each design was obtained by first splitting the design into five parts (inlet body, out 1 body, out 2 body, outer channel body, and main channel body) to obtain different element sizes for each region (ESI† S1.A). Since it was hypothesized that the main channel body would have the most complex velocity profile, a  $7\ \mu\text{m}$  element size was used to obtain more data points within this region. Moreover, a cartesian sweeping method was utilized within the main channel body mesh to facilitate velocity field analysis at individual lobes by creating evenly spaced nodes with a cartesian grid pattern. Default element sizes were used for the four remaining bodies for ease of calculation. After ensuring mesh quality, a parametric study using various inlet flow rates was conducted for each design. Simulation parameters can be found in the Materials and methods section.

For each inlet flow rate, outlet flow rates were monitored to match experimental observation. Prior to conducting a full parametric three-dimensional study on each device, two-dimensional (2D) simulations were conducted to accelerate calculation speed. To determine if the simulations roughly matched our experimental data, we first assessed the flow leaving through the device as out 1 proportional flow (out 1 flow rate/inlet flow rate). 2D simulations predicted increased out 1 proportional flow with increasing inlet flow rates, while experimental results revealed a decreasing out 1 proportional flow with increasing flow rates (ESI† S1.D). It was then hypothesized that this discrepancy could stem from the small height of the device ( $60\ \mu\text{m}$ ) significantly affecting the flow profile in the device, which 2D studies do not adequately account for. Supporting this hypothesis, three-dimensional (3D) simulations matched experimental proportional out 1

flow split results, providing more evidence of simulation accuracy.

Using known coordinates of each filter geometry, a 2D velocity profile in the main channel of the device was obtained for each flow rate across the  $x$ - $y$  plane at  $z = 30\ \mu\text{m}$ . This mid-point plane was selected to avoid drastic ceiling and floor effects. Example  $x$ -velocity contours for  $2\ \text{mL}\ \text{min}^{-1}$  and  $20\ \text{mL}\ \text{min}^{-1}$  inlet flow rates for the bent lobe design are shown in Fig. 5. As can be seen, the inlet throttle significantly increases the fluid velocity over the beginning few filter lobes from which most fluid leaves the main channel (depicted by dark blue in between the lobes). Interestingly, the lobe pore where most fluid leaves the main channel changes with inlet flow rate, likely resulting from changes in fluid inertia.<sup>47</sup> Further down the device, all simulations for both devices predict proportionally smaller transverse  $y$ -velocities between the inner and outer channels.

The most interesting result from the simulations was obtained when analyzing the  $x$ -velocity profile at  $x$ -coordinates at the edge of individual filter lobes before the downstream pore. Here, the  $x$ -velocity profile was obtained at all points in the main channel along the  $y$ -axis keeping the  $x$ -coordinate constant (portrayed by the thin, black box on velocity contour in Fig. 5). As expected, at slower inlet flow rates, the  $x$ -velocity profile mimicked Poiseuille flow commonly seen in most microfluidic flows (Fig. 5A). However, as inlet flow rates increased to greater than  $4\ \text{mL}\ \text{min}^{-1}$ , a new, complex velocity profile points emerged. At these flow rates, the  $x$ -velocity profile at each lobe had three local maxima and two inflection points, which can be visualized in Fig. 5B. Moreover, this complex velocity profile also appeared in the oblong lobe device simulations (ESI† S9).

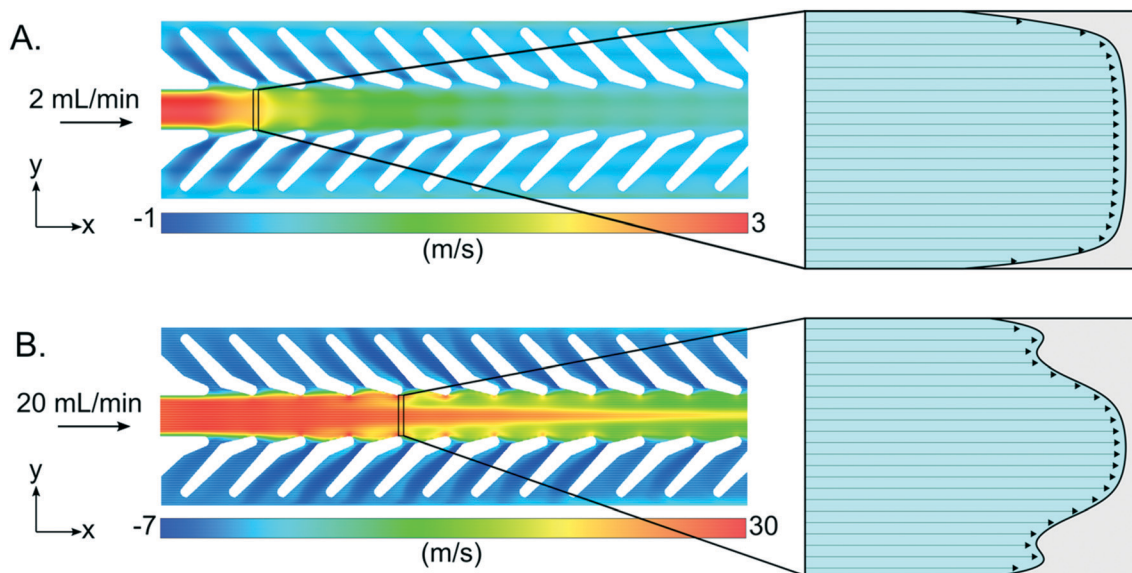


Fig. 5 Example velocity contours with main channel velocity profiles shapes at individual  $x$ -coordinates obtained from ANSYS Fluent simulations of the bent lobe design. A. A  $2\ \text{mL}\ \text{min}^{-1}$  inlet flow rate showed a classic, Poiseuille flow profile at individual lobes within the device, while the B.  $20\ \text{mL}\ \text{min}^{-1}$  inlet flow rate revealed a complex velocity profile consisting of three local velocity maxima and two inflection points.

### f. Complex velocity profiles predict filtration success

At moderate Reynold's numbers, microparticles in confined flow experience an inertial lift force due to fluid shear gradient and wake asymmetry brought by a channel wall. These forces point outward and inward from the center of the channel,<sup>8</sup> respectively. These forces are often equated to a net, inertial lift force that is dependent on the sign of the shear rate and shear gradient, among other factors.<sup>8,17,20–23</sup> Therefore, the net, inertial lift force points outward from the center channel in classic, confined Poiseuille flow. However, the complex channel design of a lobe filter greatly changes the velocity profile along the  $x$ -axis of the device, thus

significantly changing the inertial lift forces a particle experiences. Moreover, the array of lobes causes the wall-induced lift force to periodically disappear along the  $x$ -axis of the device. Without the wall-induced lift force, a particle will experience a greater outward shear-induced inertial lift force, as well as increased drag force from fluid flow in the  $y$  direction, which will cause it to pass through the filter lobes. Therefore, poor filtration would be expected if the main channel velocity profile only showed Poiseuille flow, which can be experimentally observed by the poor particle filtration with inlet flow rates under  $4 \text{ mL min}^{-1}$  (Fig. 3A and 4).

However, since the inertial lift force coefficient is proportional to the signs of shear rate and shear gradient,

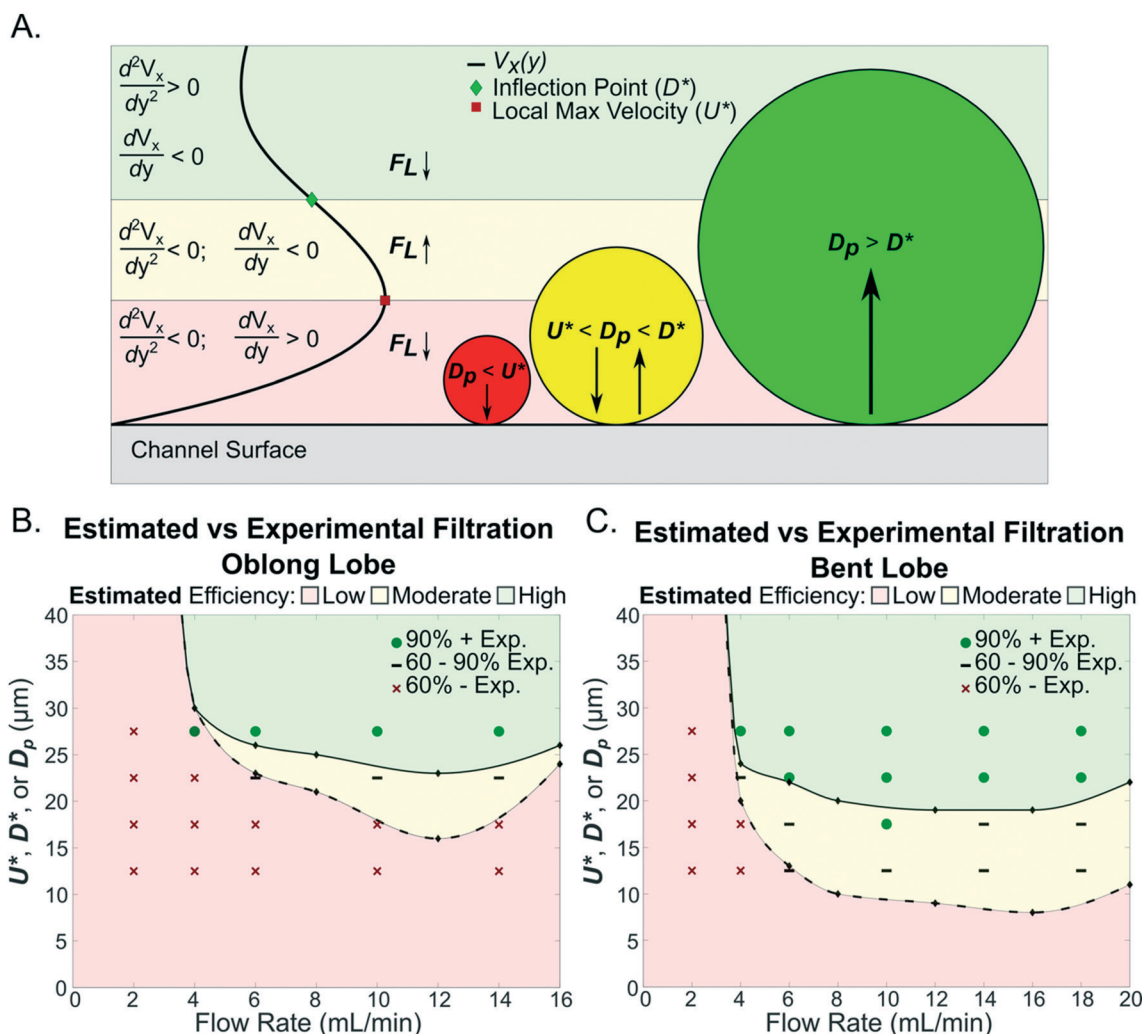


**Fig. 6** A. Cartoon representation of the inertial lift force reversal region, which is dependent on the locations of the nearest local velocity maxima and the inflection point in the velocity profile. From the channel surface to the nearest local maxima, the shear rate is positive and the shear gradient is negative, causing the inertial lift coefficient to point outward from the center of the channel. Particles small than this distance only experience outward lift force. In between the local velocity maxima ( $U^*$ ) and the inflection point ( $D^*$ ), the sign of the shear rate changes direction, which causes the inertial lift force to change directions in this region. Particles with diameters in this range may experience part of the inertial lift force direction region. Particles with diameters larger than the inflection point experience the entire lift force reversal region and thus, are filtered by the device at these lobes. Heights of the local max velocity ( $U^*$  – dashed line) and inflection point ( $D^*$  – solid line) at the lobe the lobe with the greatest outward  $y$ -velocity with experimental filtration efficiencies based on particle size ( $D_p$ ) for the B. oblong lobe design and C. bent lobe design. Particle size efficiency data was binned by low, moderate, and high efficiency depicted by the red  $x$ , dashed line, and green circle, respectively.

the net inertial lift forces a particle experience could potentially change directions in flows with inflection points.<sup>20,21</sup> Based on this hypothesis, in the range where both shear rate and shear gradient are negative, the net inertial lift force points toward the center of the main channel. This region encompasses the location of the local maxima closest to the lobe ( $U^*$ ) to the location of the inflection point ( $D^*$ ), as can be visualized in Fig. 6A (yellow shading). Therefore, we hypothesize that if a particle's diameter ( $D_p$ ) is larger than the distance from the lobe to the inflection point ( $D^*$ ), the particle will experience the lift force direction reversal. Thus, the particle will remain in the same channel and achieve high filtration efficiencies. Likewise, if  $D_p$  is less than the distance from the lobe to the height of the local maxima ( $U^*$ ), the particle is unable to experience the inertial force direction change. Hence, the particle will leave the main channel and exit through following filter pore, obtaining only low filtration efficiencies. Furthermore, if  $D_p$  is larger than  $U^*$  but smaller than  $D^*$ , the particle will not experience the full lift force reversal region. Therefore, we expect some of the particles of this size will be filtered while others will leave through filter pores, resulting in moderate filtration efficiencies.

Using this hypothesis, we were curious if we could predict lobe filtration success. Accordingly, using the velocity profiles obtained from simulations, we found the location of  $U^*$  and  $D^*$  for several inlet flow rates for both devices. For this analysis, the heights were measured at lobe locations with the highest outward secondary flow to observe the region with the strongest lateral force due to the  $y$ -velocity component, which varied by inlet flow rate. This is the location where the particles experience the strongest  $y$ -velocity resistance to remain in the main channel. Fig. 6B and C shows the locations of  $U^*$  (dashed line) and  $D^*$  (solid line) for the oblong lobe and bent lobe devices across various inlet flow rates. The estimated filtration efficiencies based on the previous hypothesis are depicted by the red, yellow, and green backgrounds. Experimental filtration efficiencies based on particle size were compared to the simulation predicted filtration success to test the viability of using  $U^*$  and  $D^*$  to explain lobe filtration results. Hence, overlaid on Fig. 6B and C are the respective experimental filtration efficiencies based on particle size ( $D_p$ ) and inlet flow rate. For ease of comparison, experimental particle size filtration efficiencies were binned and categorized into low (0–60%), moderate (60–90%), and high (>90%) efficiencies, which are depicted by a red x, black dash, and green circle, respectively.

As predicted by our theoretical analysis, the simulation-derived values for  $U^*$  and  $D^*$  predict poor filtration under 4 mL min<sup>-1</sup> for both devices due to the lack of inflection points in the velocity profiles, which is recapitulated by the experimentally determined values. However, at inlet flow rates above 4 mL min<sup>-1</sup>, predicted filtration success varies between both devices. At each inlet flow rate,  $D^*$  for the oblong lobe device is higher than the  $D^*$  for the bent lobe

device with a minimum  $D^*$  of 23  $\mu\text{m}$  for the oblong lobe device and 19  $\mu\text{m}$  for the bent lobe. Thus, these differences in  $D^*$  predicted a larger  $D_p$  necessary for high efficiency filtration in the oblong lobe device. The estimated efficiencies are supported by the experimentally obtained filtration efficiencies, as the oblong lobe device only obtained high efficiencies with the 25–30  $\mu\text{m}$  bin, while the bent lobe device obtained high efficiencies down to the 15–20  $\mu\text{m}$  bin. Additionally, the channel location where the inertial lift force points inward, or the area indicated by the yellow in both figures, is predicted to be much smaller for the oblong lobe device, which would predict fewer particle sizes that are able to obtain moderate filtration efficiencies. Again, the experimental values support the predicted values, as the oblong device only obtained moderate efficiencies at three inlet flow rates for the 20–25  $\mu\text{m}$  particle size bin. Moreover, the oblong lobe simulation predicted a higher  $U^*$  at each inlet flow rate than the bent lobe device with a minimum at 17  $\mu\text{m}$  compared to 10  $\mu\text{m}$  for the bent lobe device. The predicted values are further supported by the low efficiencies obtained by all particles under 20  $\mu\text{m}$  in the oblong lobe device. Conversely, the bent lobe device obtained moderate efficiencies with the 10–15  $\mu\text{m}$  bin for all inlet flow rates over 6 mL min<sup>-1</sup>. Interestingly, both device simulations predicted a slight increase in both  $U^*$  and  $D^*$ , at the filter's maximum inlet velocity, which may suggest decreased filtration success at inlet flow rates higher than tested. Remarkably, experimental filtration efficiencies match very well with the simulation-estimated efficiencies for both devices, which strongly supports that simulation-derived distances for the inertial lift force reversal region can be used to predict microfluidic lobe filtration success.

## 4. Conclusions

Microfluidic microparticle filtration is often a slow and tedious process plagued with filter clogging and slow flow rates. Lobe filtration, bioinspired by the manta ray's filter feeding mechanism, offers a unique solution for these issues. As a novel mechanism for microfluidic applications, lobe filtration offers high throughput microparticle filtration with processing speeds up to 20 mL min<sup>-1</sup>. The high processing speeds open the possibility for various applications in which large volumes of liquid need to be filtered. For example, microplastic removal, which has concentrations of ~400 parts per L,<sup>4,48</sup> would otherwise not be possible using a microfluidic device without extensive parallelization. Moreover, lobe filtration offers high sample filtrate purity (>98%), making it promising solution for applications such as tissue dissociation and filtration of MCF-7 human cancer cells and murine kidney tissue cells.<sup>36</sup> Lobe filtration also enables microparticle concentration up to a factor of 2.05 at 10 mL min<sup>-1</sup>, which would similarly increase throughput of sample concentrations of dilute microparticle suspensions.

Remarkably, lobe filtration success can be estimated through a simple analysis of the velocity profiles within the

device. Understanding that the inertial lift force may change directions in the presence of an inflection point in the bulk velocity profile, microparticle filtration success can be estimated by comparing the particle size to the distance from a filter lobe with the highest transverse velocity to the inflection point in bulk flow. We have shown that this method of predicting filtration success works for both filter lobe designs over various inlet flow rates. Quick visualization of  $U^*$  and  $D^*$  for both devices reveal that the bent lobe device will provide better filtration efficiencies compared to the oblong lobe design since its high efficiency area (green shading) in Fig. 6 is larger and its low efficiency area (red shading) is smaller. Using this method, lobe filter designs can be tuned to optimize the bulk flow inflection point location and thus filter or concentrate particles of desired sizes at ultra-high throughputs.

## Conflicts of interest

There are no conflicts to declare.

## Acknowledgements

This work was supported by the U.S. National Science Foundation (IOS 1838314) and the NIH (R21AG059099).

## References

- M. S. Maria, B. S. Kumar, T. S. Chandra and A. K. Sen, Development of a microfluidic device for cell concentration and blood cell-plasma separation, *Biomed. Microdevices*, 2015, **17**, 1–19.
- H. W. Hou, *et al.*, Microfluidic devices for blood fractionation, *Micromachines*, 2011, **2**, 319–343.
- T. Tachi, N. Kaji, Y. Okamoto, M. Tokeshi and Y. Baba, Simultaneous separation, metering and dilution of plasma from human whole blood using a microchip with an interchannel microstructure, *Proc. Conf. MicroTAS 2009 – 13th Int. Conf. Miniaturized Syst. Chem. Life Sci.*, 2009, vol. 81, pp. 427–429.
- J. Li, H. Liu and J. Paul Chen, Microplastics in freshwater systems: A review on occurrence, environmental effects, and methods for microplastics detection, *Water Res.*, 2018, **137**, 362–374.
- J. Talvitie, M. Heinonen, A. Koistinen and A. Mikola, How well is microlitter purified from wastewater? A detailed study on the stepwise removal of microlitter in a tertiary level wastewater treatment plant, *Water Res.*, 2017, **109**, 164–172.
- E. Dressaire and A. Sauret, Clogging of microfluidic systems, *Soft Matter*, 2017, **13**, 37–48.
- D. C. Duffy, J. C. McDonald, O. J. A. Schueller and G. M. Whitesides, Rapid prototyping of microfluidic systems in poly(dimethylsiloxane), *Anal. Chem.*, 1998, **70**, 4974–4984.
- D. Di Carlo, Inertial microfluidics, *Lab Chip*, 2009, **9**, 3038–3046.
- X. Ding, *et al.*, Cell separation using tilted-angle standing surface acoustic waves, *Proc. Natl. Acad. Sci. U. S. A.*, 2014, **111**, 12992–12997.
- Y. Akiyama, T. Egawa, K. Koyano and H. Moriwaki, Acoustic focusing of microplastics in microchannels: A promising continuous collection approach, *Sens. Actuators, B*, 2020, **304**, 127328.
- M. Hejazian, W. Li and N. Nguyen, Lab on a chip for continuous-flow magnetic cell separation, *Lab Chip*, 2015, **15**, 959–970.
- L. R. Huang, E. C. Cox, R. H. Austin and J. C. Sturm, Continuous Particle Separation Through Deterministic Lateral Displacement, *Science*, 2004, **304**, 987–990.
- X. Chen, D. F. Cui, C. C. Liu and H. Li, Microfluidic chip for blood cell separation and collection based on crossflow filtration, *Sens. Actuators, B*, 2008, **130**, 216–221.
- H. Y. Li, C. D. Bertram and D. E. Wiley, Mechanisms by which pulsatile flow affects cross-flow microfiltration, *AIChE J.*, 1998, **44**, 1950–1961.
- Y. Yoon, *et al.*, Clogging-free microfluidics for continuous size-based separation of microparticles, *Sci. Rep.*, 2016, **6**, 1–8.
- A. Lenshof and T. Laurell, Continuous separation of cells and particles in microfluidic systems, *Chem. Soc. Rev.*, 2010, **39**, 1203–1217.
- D. Stoecklein and D. Di Carlo, Nonlinear Microfluidics, *Anal. Chem.*, 2019, **91**, 296–314.
- Q. Zhao, D. Yuan, J. Zhang and W. Li, A review of secondary flow in inertial microfluidics, *Micromachines*, 2020, **11**, 1–23.
- L. Wang and D. S. Dandy, High-Throughput Inertial Focusing of Micrometer- and Sub-Micrometer-Sized Particles Separation, *Adv. Sci.*, 2017, **4**, 1700153.
- B. P. Ho and L. G. Leal, Inertial migration of rigid spheres in two-dimensional unidirectional flows, *J. Fluid Mech.*, 1974, **65**, 365–400.
- H. Amini, W. Lee and D. Di Carlo, Inertial microfluidic physics, *Lab Chip*, 2014, **14**, 2739–2761.
- C. Liu, C. Xue, J. Sun and G. Hu, A generalized formula for inertial lift on a sphere in microchannels, *Lab Chip*, 2016, **2016**, 884–892.
- E. S. Asmolov, The inertial lift on a spherical particle in a plane poiseuille flow at large channel Reynolds number, *J. Fluid Mech.*, 1999, **381**, 63–87.
- B. Kwak, *et al.*, Hydrodynamic blood cell separation using fishbone shaped microchannel for circulating tumor cells enrichment, *Sens. Actuators, B*, 2018, **261**, 38–43.
- A. Özbey, M. Karimzadehkhoei, H. Alijani and A. Koşar, Microparticle Inertial Focusing in an Asymmetric Curved Microchannel, *Fluids*, 2018, **3**, 57.
- X. Wang, J. Zhou and I. Papautsky, Vortex-aided inertial microfluidic device for continuous particle separation with high size-selectivity, efficiency, and purity, *Biomicrofluidics*, 2013, **7**, 044119.
- A. Volpe, P. Paiè, A. Ancona and R. Osellame, Polymeric fully inertial lab-on-a-chip with enhanced-throughput sorting capabilities, *Microfluid. Nanofluid.*, 2019, **23**, 1–10.
- M. E. Warkiani, *et al.*, Malaria detection using inertial microfluidics, *Lab Chip*, 2015, **15**, 1101–1109.

- 29 D. Di Carlo, J. F. Edd, K. J. Humphry, H. A. Stone and M. Toner, Particle segregation and dynamics in confined flows, *Phys. Rev. Lett.*, 2009, **102**, 1–4.
- 30 A. A. S. Bhagat, S. S. Kuntaegowdanahalli and I. Papautsky, Inertial microfluidics for continuous particle filtration and extraction, *Microfluid. Nanofluid.*, 2009, **7**, 217–226.
- 31 S. Shen, *et al.*, Spiral microchannel with ordered micro-obstacles for continuous and highly-efficient particle separation, *Lab Chip*, 2017, **17**, 3578–3591.
- 32 B. Tasadduq, W. Lam, A. Alexeev, A. F. Sarioglu and T. Sulchek, Enhancing size based size separation through vertical focus microfluidics using secondary flow in a ridged microchannel, *Sci. Rep.*, 2017, **7**, 1–10.
- 33 I. D. Johnston, *et al.*, Dean flow focusing and separation of small microspheres within a narrow size range, *Microfluid. Nanofluid.*, 2014, **17**, 509–518.
- 34 A. Mihandoust, *et al.*, High-throughput particle concentration using complex cross-section microchannels, *Micromachines*, 2020, **11**, 440.
- 35 J. H. Lee, S. K. Lee, J. H. Kim and J. H. Park, Separation of particles with bacterial size range using the control of sheath flow ratio in spiral microfluidic channel, *Sens. Actuators, A*, 2019, **286**, 211–219.
- 36 X. Qiu, *et al.*, Microfluidic filter device with nylon mesh membranes efficiently dissociates cell aggregates and digested tissue into single cells, *Lab Chip*, 2018, **18**, 2776–2786.
- 37 X. Qiu, *et al.*, Microfluidic channel optimization to improve hydrodynamic dissociation of cell aggregates and tissue, *Sci. Rep.*, 2018, **8**, 1–10.
- 38 R. V. Divi, J. A. Strother and E. W. M. Paig-Tran, Manta rays feed using ricochet separation, a novel nonclogging filtration mechanism, *Sci. Adv.*, 2018, **4**, eaat9533.
- 39 E. W. M. Paig-Tran, T. Kleinteich and A. P. Summers, The filter pads and filtration mechanisms of the devil rays: Variation at macro and microscopic scales, *J. Morphol.*, 2013, **274**, 1026–1043.
- 40 E. W. M. Paig-tran, J. J. Bizzarro, J. A. Strother and A. P. Summers, Bottles as models : predicting the effects of varying swimming speed and morphology on size selectivity and filtering efficiency in fishes, *J. Exp. Biol.*, 2011, **214**, 1643–1654.
- 41 E. J. Mossige, A. Jensen and M. M. Mielnik, An experimental characterization of a tunable separation device, *Microfluid. Nanofluid.*, 2016, **20**, 1–10.
- 42 E. J. Mossige, A. Jensen and M. M. Mielnik, Separation and Concentration without Clogging Using a High-Throughput Tunable Filter, *Phys. Rev. Appl.*, 2018, **9**, 54007.
- 43 E. J. Mossige, B. Edvardsen, A. Jensen and M. M. Mielnik, A tunable, microfluidic filter for clog-free concentration and separation of complex algal cells, *Microfluid. Nanofluid.*, 2019, **23**, 1–13.
- 44 J. Ding, S. Zhang, R. M. Razanajatovo, H. Zou and W. Zhu, Accumulation, tissue distribution, and biochemical effects of polystyrene microplastics in the freshwater fish red tilapia (*Oreochromis niloticus*), *Environ. Pollut.*, 2018, **238**, 1–9.
- 45 J. P. G. L. Frias and R. Nash, Microplastics: Finding a consensus on the definition, *Mar. Pollut. Bull.*, 2019, **138**, 145–147.
- 46 R. Ozawa, H. Iwadate, H. Toyoda, M. Yamada and M. Seki, A numbering-up strategy of hydrodynamic microfluidic filters for continuous-flow high-throughput cell sorting, *Lab Chip*, 2019, **19**, 1828–1837.
- 47 S. Blonski, *et al.*, Impact of inertia and channel angles on flow distribution in microfluidic junctions, *Microfluid. Nanofluid.*, 2020, **24**, 14.
- 48 M. A. Browne, *et al.*, Accumulation of microplastic on shorelines worldwide: Sources and sinks, *Environ. Sci. Technol.*, 2011, **45**, 9175–9179.
- 49 L. Clime, *et al.*, Microfluidic filtration and extraction of pathogens from food samples by hydrodynamic focusing and inertial lateral migration, *Biomed. Microdevices*, 2015, **17**, 17.